J Nanopart Res (2012) 14:667
DOI 10.1007/s11051-011-0667-6

RESEARCH PAPER

Morphologically different WO_3 nanocrystals in photoelectrochemical water oxidation

Soumya Kanti Biswas · Jin-Ook Baeg · Sang-Jin Moon · Ki-jeong Kong · Won-Wook So

Received: 24 August 2011 / Accepted: 22 December 2011 / Published online: 17 January 2012

Abstract Different morphologies of WO_3 nanocrystals such as nanorods and nanoplates have been obtained under hydrothermal conditions using ammonium metatungstate as the precursor in presence of different organic acids such as citric, oxalic, and tartaric acid in the reaction medium. Detailed characterization of the crystal structure, particle morphology, and optical band gap of the synthesized powders have been done by X-ray diffraction, transmission electron microscopy, scanning electron microscopy and solid-state UV–visible spectroscopy study. The as-synthesized materials are WO_3 hydrates with orthorhombic phase which transform to the hexagonal WO_3 through dehydration upon heating at 350 °C. The resultant products are crystalline with nanoscale dimensions. Finally, the photoactivity of the synthesized materials annealed at 500 °C has been compared employing in photoelectrochemical water oxidation under the illumination of AM 1.5G simulated solar light (100 $mWcm^{-2}$). The photocurrent measurements upon irradiation of light exhibit obvious photocatalytic activity with a photocurrent of about 0.77, 0.61, and 0.65 $mAcm^{-2}$ for the WO_3 film derived with the oxalic acid, tartaric, and citric acid assisting agents, respectively, at 1.8 V versus Ag/AgCl electrode.

Keywords WO_3 nanocrystals · Nanorod and nanoplate morphologies · Structure-directing agents · Hydrothermal conditions · Photoelectrochemical water oxidation

Introduction

Tungsten oxide (WO_3) is a widely investigated transition metal oxide due to its potential applications in heterogeneous catalysis (Zhao et al. 2010), gas sensors (Li et al. 2004; Lin et al. 1994), electrochromic and optochromic devices (Lee et al. 2006; Takeda et al. 2004), and dye-sensitized solar cells (Zheng et al. 2010). WO_3 is an *n*-type semiconductor which has also been recognized as an active visible-light-driven photoanode material for photoelectrochemical (PEC) water splitting since 1976 (Hodes et al. 1976). The properties that have made WO_3 imperative in current PEC research include good stability in water (<pH 4), photostability, suitable band gap energy (around 2.6 eV) for considerable absorption within the solar spectrum, energetically favorable valence band position for water oxidation, and excellent electron transport property along with hole diffusion length around 150 nm (Butler 1977; Bamwenda and

Electronic supplementary material The online version of this article (doi:10.1007/s11051-011-0667-6) contains supplementary material, which is available to authorized users.

S. K. Biswas · J.-O. Baeg (✉) · S.-J. Moon · K. Kong · W.-W. So
Advanced Chemical Technology Division, Korea Research Institute of Chemical Technology, Yusong, Daejeon 305-600, Republic of Korea
e-mail: jobaeg@krict.re.kr

Arakawa 2001; Kominami et al. 2001; Wang et al. 2000; Santato et al. 2001).

Morphology control of metal oxides has been a focus of recent research interest because the morphology of the nanostructures has a significant effect on their properties and applications (Zhou et al. 2008a, b). The morphology of the particles is greatly influenced by the method of preparation, the initial precursor, type of the chemicals used, and control of the experimental parameters. The syntheses of morphology-controlled WO_3 and WO_3 hydrate nanostructures, as for examples, nanowires (Li et al. 2003), nanorods (Lee et al. 2003; Gu et al. 2005), nanotubes (Zhao and Miyauchi 2008), and hexagonal-shaped nanodiscs (Zhou et al. 2008a) are reported in the literature. They have been prepared by high-temperature evaporation, precipitation, hydrothermal reaction, electrochemical or template-assisted routes. Hydrothermal synthesis is a facile, cost-effective, single-step low-temperature approach which can successfully be used in morphology-tailored synthesis by introducing suitable structure-directing mediator under the controlled reaction conditions. Some of these WO_3 or WO_3 hydrate materials with controlled morphologies have been demonstrated for their photocatalytic activities. Recently, few reports have been published on the photooxidation of water using hydrothermally grown WO_3 nanoparticles (Hong et al. 2009; Amano et al. 2010; Su et al. 2011; Jiao et al. 2011). However, there is a scope to investigate the photocatalytic activity of WO_3 with different morphologies.

The WO_3 hydrates are the parent materials of WO_3. Generally, the WO_3 hydrates are produced first in liquid-phase synthesis routes and subsequently annealed to obtain the desired crystal phase of WO_x (Zheng et al. 2011). Transformation and structural relationships of the metastable WO_3 hydrates to the desired crystal phase such as hexagonal WO_3 lead to a *chimie douce* studies (Michailovski et al. 2004). Herein, we demonstrate a simple hydrothermal condition to realize the morphology-controllable synthesis of the crystalline tungsten oxide hydrates which convert to hexagonal WO_3 with nanosize dimension upon subsequent thermal treatment. We report for the first time the synthesis of different morphologies of tungsten oxide hydrates from ammonium metatungstate precursor employing different organic acids such as citric, oxalic, and tartaric acid as structure-directing agents. The structure-directing agents are known to dynamically modify the growth rate of the nanoparticles either by promoting or inhibiting the crystal growth satisfying the surface energy requirements for each surface along specific crystallographic planes. Detailed characterization of the crystal structure and particle morphology of the synthesized powders has been done in this work. The photoactivity of the synthesized powders in dehydrated form assembled on F doped SnO_2 (FTO) coated glass substrate through film casting has been compared for photoelectrochemical water oxidation under the standard condition air mass 1.5 global (AM 1.5 G) at 100 $mWcm^{-2}$.

Experimental section

Materials used

Ammonium metatungstate, citric acid, oxalic acid, D-tartaric acid, and H_2SO_4 were used chemicals in the present study. All the chemicals used were of analytical grade procured from Aldrich, except ammonium metatungstate which was purchased from Fluka. Ultrapure water (18.2 MΩcm) from a Milli-Q water system was used throughout the experiments.

Material preparation

The nanocrystalline WO_3 hydrate was synthesized from ammonium metatungstate ($(NH_4)_6H_2W_{12}O_{40}$, AMT) as tungsten precursor by a simple hydrothermal reaction. The reactions were carried out using different carboxylic acids as structure-directing agents. In a typical synthesis, oxalic acid (2.52 g) was dissolved in 40 mL water by gentle heating. AMT (2.46 g) was then dissolved in aqueous solution of oxalic acid under stirring at room temperature. After achieving complete dissolution, the solution was transferred to a Teflon-lined stainless-steel autoclave. The hydrothermal reaction was carried out at a constant temperature of 180 °C without stirring for 24 h. After reaction, the autoclave was allowed to cool down naturally to room temperature. The precipitate was filtered, washed with distilled water several times to remove ions that possibly remained in the final products, and dried at 50 °C. The molar ratio of the tungsten content to the organic acids was maintained at 1:2 in all the syntheses. The WO_3 hydrate was then subjected to heat treatment at 350 °C in static air using a programmable furnace with heating rate of 5 °C min^{-1} to obtain WO_3 nanocrystals with hexagonal crystal phase.

Electrode fabrication

The photoactivity of the synthesized powders was investigated in photoelectrochemical oxidation of water. The working electrodes were fabricated over F doped SnO_2 (FTO) coated glass substrate using the synthesized oxides by doctor's blade spreading technique for the electrochemical measurements. Before coating the film, the FTO glass substrates were cleaned using distilled water, ethanol, and acetone by ultrasonication for degreasing and dried under N_2 flow. The paste was prepared by drenching 0.25 g of the synthesized powders with 50 μL of 10% acetylacetone in hexanol and then dispersing in 2.5 mL of 1% acetylacetone in 2-propanol under sonication for 30 min. 0.1 g hydroxypropyl cellulose was mixed with this suspension under magnetic stirring for overnight. 50 μL of the suspension was dropped onto 1 cm × 1 cm area of the FTO glass substrate left open applying scotch tape and the slurry dispersed over the open space of the FTO glass daintily using a glass slide. After drying at room temperature and removing the scotch tape blockade, the FTO glass with coated film was dried at 80 °C for 1 h and then annealed at 500 °C for 1 h in air using a programmable furnace with heating rate of 5 °C min^{-1} to combust the binder. After that the uncovered portion of the FTO substrate was connected to a copper wire by silver paste to make ohmic contact. Finally, the portion of silver paste and bare part of the FTO substrate were covered with epoxy resin to isolate those areas from an aqueous electrolyte solution. In order to study the effect of the annealing temperature on the photoanodic behavior, a series of oxalic acid-assisted WO_3 films coated over FTO glass were annealed in air at different temperatures ranging from 450 to 600 °C for 1 h.

Characterization

The phase analysis of the as-synthesized powders as well as of the films prepared employing the as-synthesized powders was performed by X-ray diffraction (XRD) study using a Rigaku-D/MaX-2200V X-ray diffractometer Cu-Kα radiation ($\lambda = 1.5416$ Å) and Ni filter with the X-ray tube set to 40 kV and 40 mA at room temperature. The crystallite size of the samples was calculated using Scherrer's equation to the full-widths at half-maximum (FWHM) of the diffraction peaks. The actual FWHMs were calculated considering the peaks to be of the Gaussian type. The morphological characterization of the as-synthesized powders and the films were carried out using scanning electron microscope (SEM) [Model: JEOL-JSM 6700F Field emission (FE) SEM and Philips XL30S SEM FEG with an accelerating voltage of 15 and 10 kV, respectively]. The particles morphologies of the as-synthesized powders were also studied by transmission electron microscope (TEM) (Model: TECNAIG^{2}T-20S FEI, 200 kV). One or two drops of sonicated samples in ethanol taken on carbon-coated copper grid were employed to the TEM investigations. Optical properties were studied with a UV–visible diffuse reflectance spectrometer with a Shimadzu spectrophotometer (Model: UV-2450) using $BaSO_4$ as a reference. The optical properties of the synthesized powders were measured after preparing the films. The films were cast onto glass substrates by spreading the slurry of the as-synthesized powders and annealed for the XRD, SEM, and the optical property studies. Simultaneously recorded thermogravimetric and differential thermal analysis (TGA-DTA) of the as-synthesized powders and the slurry prepared for coating the films were carried out in air at a heating rate of 10 °C min^{-1} using TA Instruments (Model: SDT 2960).

The photoelectrochemical measurements of the films were conducted in a standard single-compartment three-electrode electrochemical home-built cell equipped with Ag/AgCl (3 M KCl) reference electrode, a platinum wire as a counter electrode, and the WO_3 film-coated FTO working electrode using an electrochemical analyser (CH Instrument, Model: CHI 1100A). An electrolyte solution of 0.5 M H_2SO_4 (pH ~0.3) was used for all the electrochemical measurements. The photocurrent–potential curves were recorded using simulated solar spectrum designed by a solar simulator (Newport 69911, power supply) with AM 1.5G filter. All the photoelectrochemical experiments were carried out under argon atmosphere at 25 °C. For the measurement of incident photon-to-current conversion efficiency (IPCE), a 450-W xenon lamp light source (Newport) with 80 mm water filter to avoid IR and a monochromator for the wavelength selection were used. Photon flux was measured by an optical power meter (Oriel 69920).

Results and discussion

The XRD patterns of the as-synthesized WO_3 hydrates powders obtained from the hydrothermal reactions are

shown in Fig. 1. The as-synthesized powders obtained in presence of different organic acids exhibited very similar XRD patterns. The products identified were predominantly crystalline WO_3 hydrates, as the majority of the peaks were well matched with the diffraction lines of the orthorhombic tungsten oxide hydrate (WO_3 $0.33H_2O$) (JCPDS 97-001-5514) as shown in the figure. The peak at $2\theta = 13.9°$ which corresponds to (020) plane for the orthorhombic phase of WO_3 hydrate was found to be consisting of two peaks merged together as seen in the figure. The presence of small amount of NH_4^+ containing WO_3 species which was found to be comparable to $(NH_4)_{0.33-x}WO_{3-z}$ species (JCPDS 00-058-0151) could not be ruled out. The similar observation, that is, strong adsorption bonding for NH_4^+ species onto the WO_3 was detected in X-ray photoelectron spectroscopy (XPS) study in a previous literature report (Zhu et al. 2011) where WO_3 was prepared from ammonium tungstate precursor. Further washing the as-prepared powders with water and immersing in 1 N H_2SO_4 for 12 h, and subsequent rinsing with water were not effective to eliminate the second peak from the (020) peak of orthorhombic tungsten oxide hydrates (S1a). However, the second peak was not detected in the synthesized material after heating of the powders as seen in the figure (S1b) which may suggest the desorption of NH_4^+ species after the heat treatment at 350 °C for 1 h (S1c, d). Li's group also

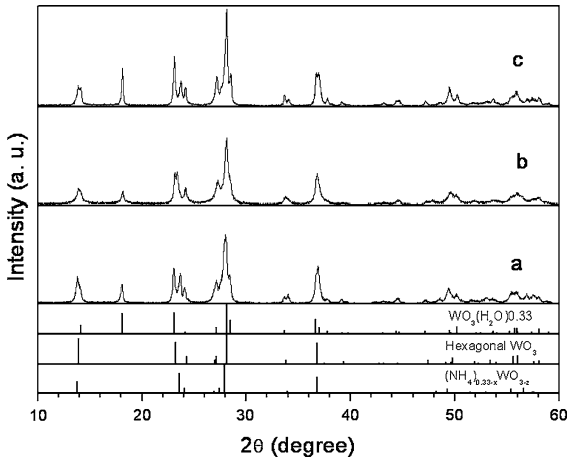

Fig. 1 XRD patterns of the as-synthesized WO_3 hydrates prepared in the presence of *a* oxalic acid, *b* citric acid, and *c* tartaric acid. PDF number of the standard XRD data of $WO_3(H_2O)0.33$, hexagonal WO_3, and $(NH_4)_{0.33-x}WO_{3-z}$ are 97-001-5514, 97-008-0635, and 00-058-0151, respectively

reported a similar observation (Zhu et al. 2011). The orthorhombic phase disappeared and hexagonal phase of the synthesize material was formed after extending duration of heating at 350 °C for 5 h (S1e). Crystal transformation to the hexagonal WO_3 proceeded through dehydration of hydroxyl groups in the crystalline WO_3 hydrates. Nanostructured WO_3 with orthorhombic crystal phase obtained by post annealing retained its phase stability at room temperature (Zheng et al. 2011).

Thermal analysis offered evidence of overall ~5% weight loss of the as-obtained WO_3 hydrate in the temperature range from 23 to 450 °C. The TG profile of WO_3 hydrate obtained by oxalic acid-assisted route in S2a displayed two weight loss steps: the first weight loss of about 2.22% occurred up to 200 °C which could correspond mainly to the removal of adsorbed water. The second weight loss of about 2.78% between 200 and 450 °C recorded in the TG profile could be associated with the loss of structural water. A similar thermal behavior was observed by Sediri's group (Boukriba et al. 2010). The DTA curve recorded in the present study shown in S2a evidenced a well-defined endothermic peak with minima at around 45 °C followed by a weak, ill-defined endothermic peak centered at around 100 °C due to elimination of water.

SEM and TEM analysis provided the direct information of microstructure and morphology of the nanoparticles prepared by hydrothermal reactions. They offered comparable information for morphology and size of the analyzed materials. The typical SEM images of the WO_3 hydrates are depicted in Fig. 2a, c, e. The SEM studies revealed that the WO_3 hydrates obtained by the hydrothermal synthesis in the presence of oxalic and citric acid exhibited nanosized rod-like morphology. However, a noticeable difference in morphologies of the oxalic- and citric acid-assisted products could be witnessed. A large portion of the oxalic acid-assisted product in SEM image (Fig. 2a) clearly evidenced that the particles were mostly of one-dimensional nanostructure with around 25 nm of width and up to 400 nm in length, whereas the citric acid-assisted product was observed to contain nanorod particles with some nanosheet patterns as depicted in Fig. 2c. The width of the nanorods of citric acid-mediated WO_3 hydrate products was less than 100 nm and the length was around 1–2 μm, and the width of the nanorods was found broadly distributed. Mostly

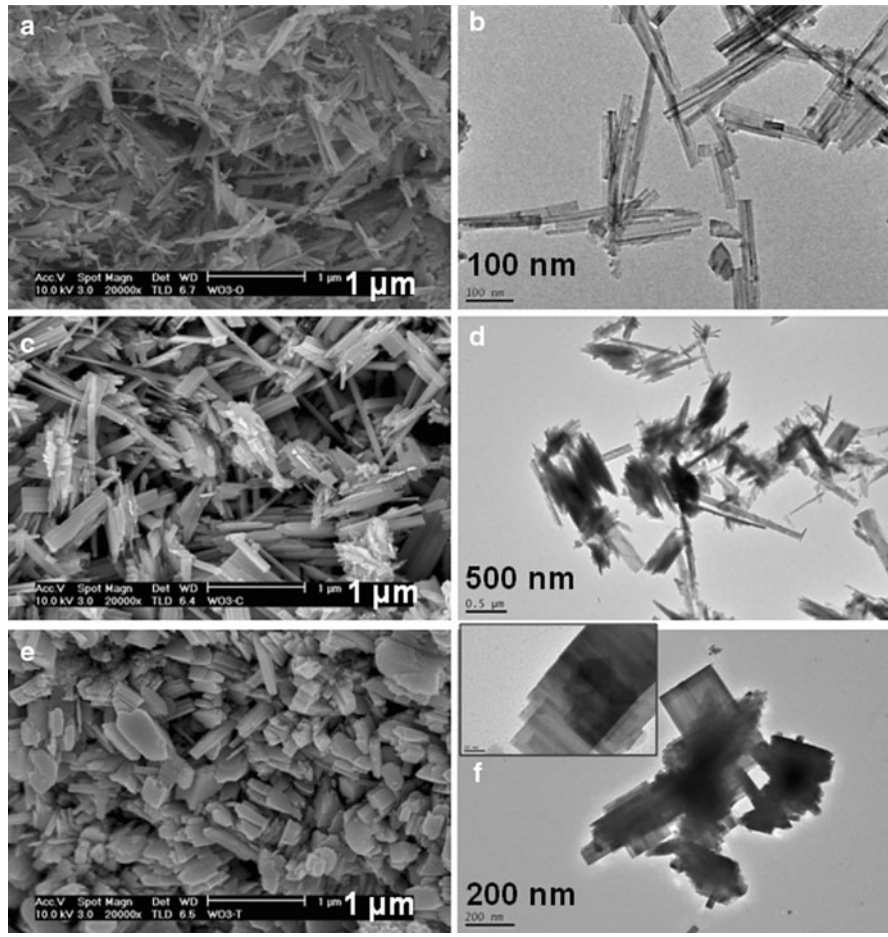

Fig. 2 SEM (**a**, **c**, and **e**) and TEM images (**b**, **d**, and **f**) of the as-synthesized WO_3 hydrates prepared in the presence of oxalic acid (**a**, **b**), citric acid (**c**, **d**), and tartaric acid (**e**, **f**). High-resolution TEM image (*inset*) of WO_3 hydrates prepared in the presence of tartaric acid

plate-like morphology with varying edge length ranging from 50 to 200 nm in irregular order was noticed in SEM micrograph (Fig. 2e) when tartaric acid was used as an assistant agent in synthesis. The plate-like particles showed the flat surface characteristics. Some portions of the nanostructures were found to be self-assembled layers with varying thickness. The structures of the products after thermal treatment at 350 °C are presented in the magnified SEM images inserted in Fig. 3a, c, and e, which depict no noticeable alternation of the morphology observed after heating.

For further study of the morphological and microstructural details of the resultant products the TEM experiment was carried out. Figure 2b, d, and f show representative TEM images of the WO_3 hydrates, prepared in the presence of different organic acids by hydrothermal approaches. The observed morphologies were consistent with those from the SEM images. The TEM study exhibited that the oxalic acid-mediated synthesis gave rise to predominantly rod-like morphology of the WO_3 hydrates with width less than 25 nm and length up to 400 nm indicating the formation of one-dimensional nanostructures with high-aspect ratio in high yield (Fig. 2b). The obtained one-dimensional nanostructures had a narrow size distribution of width. The citric acid-assisted synthesis under similar hydrothermal conditions resulted in nanorod shape with some nanosheet patterns. The width and length of the nanorods of WO_3 hydrate were found to be less than 100 nm and around 1–2 µm, respectively. The sheet-like particles were observed with varying edge length (Fig. 2d). The tartaric acid-controlled synthesis produced nanoplate morphology with wide surface. The self-assembly of layers was

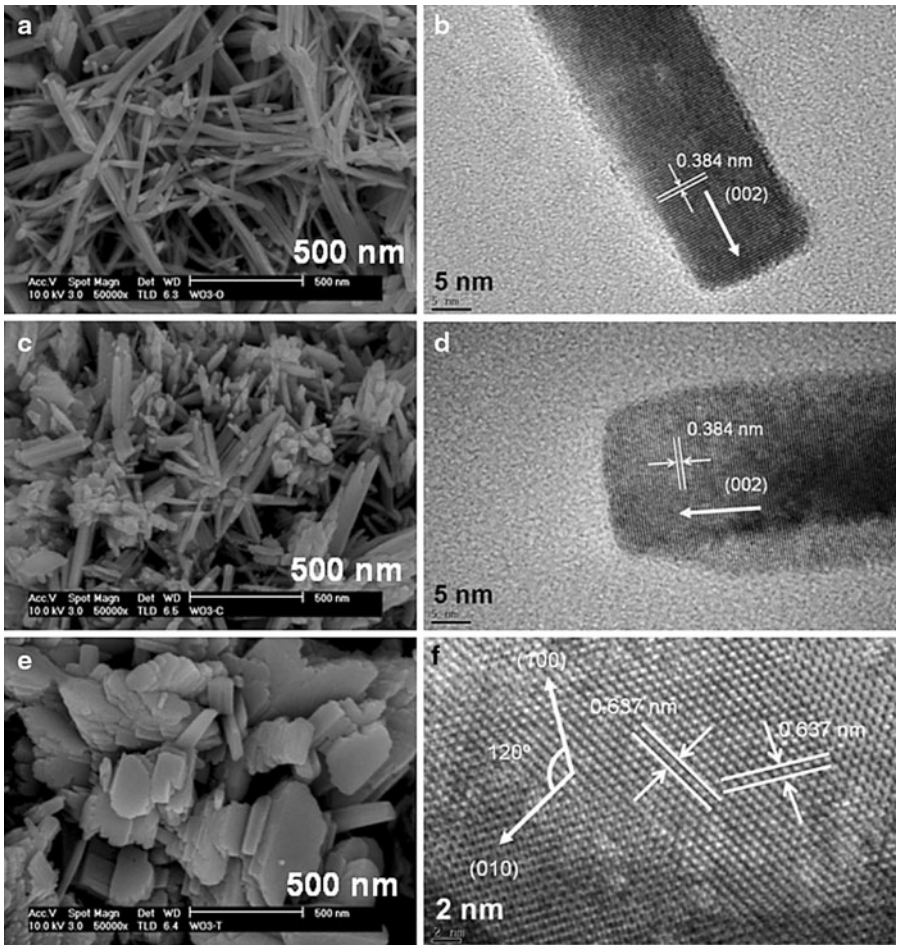

Fig. 3 SEM (**a**, **c**, and **e**) (with high magnification) and HRTEM images (**b**, **d**, and **f**) of the WO_3 prepared in the presence of oxalic acid (**a**, **b**), citric acid (**c**, **d**), and tartaric acid (**e**, **f**) and heat-treated at 350 °C for 5 h

noticed by TEM experiment (Fig. 2f). Some of the particles were witnessed having square or rectangular morphologies as seen in Fig. 2f (inset).

A high-resolution (HR) TEM image of a single nanowire with diameter of about 15 nm (Fig. 3b) presented further insight into the structure of the WO_3 nanorods prepared in the presence of oxalic acid and heat treated at 350 °C. The lattice fringes in the HRTEM micrographs indicated the crystalline nature of the product. The XRD study suggested the hexagonal crystal phase of the materials after heat treatment at 350 °C. The lattice spacing of about 0.384 nm between adjacent lattice planes, as examined from the HRTEM image corresponded to the d-spacing of (002) planes of the hexagonal phase of WO_3. The (002) planes were found to be perpendicular to the direction of growth of the nanorods suggesting that the nanorods grew along (002) direction (*c*-axis). A similar observation for one-dimensional WO_3 was reported in the previous literature (Rajagopal et al. 2009). The citric acid-mediated nanorod products after heat treatment at 350 °C showed the lattice spacing of about 0.38 nm in HRTEM image (Fig. 3d) which is comparable to the d-spacing value of (002) planes of the hexagonal crystal phase of WO_3 indicating the growth direction along (002) direction (*c*-axis). The HRTEM image (Fig. 3f) for WO_3 plates prepared in presence of tartaric acid and heated at 350 °C displayed (100) and (010) planes with an angle of 120° corresponding to almost the same lattice spaces of around 0.637 nm with a hexagonal phase as was shown by Zhu et al. (2011) in their report.

Obviously, the organic acids play a role in shaping the morphology of the synthesized products under hydrothermal condition. Oxalic acid has two carboxyl (–COOH) groups, citric acid has three –COOH and one hydroxyl (–OH) groups, while tartaric acid has two –COOH and two –OH groups. These polycarboxylic,

hydroxy-polycarboxylic, and polyhydroxy–polycarboxylic acids are known to form chelates with tungsten species with –O–W–O– linkage in aqueous solutions stabilizing acidic tungsten solutions and preventing polycondensation (Lassner and Schubert 1999). Both carboxyl and hydroxyl groups of hydroxycarboxylic acid have been detected to participate in the formation of mono and dinuclear complexes with W(VI) species (Llopis et al. 1986). All these acids are dispersant for tungsten species in aqueous solutions. In the early stage of the hydrothermal process nuclei of WO_3 hydrates were formed. This stage is followed by the crystal growth process. The nucleation rate is modified by the presence of carboxylic acid complexes. The acids bind selectively onto the particular facets of the freshly formed tungsten oxide hydrate seed particles and stabilize the specific planes. The alternation in the order of free energies of different facets of seed surface through this strong and weak binding of organic acid to the crystal planes influence the relative growth of different facets (Xiong and Xia 2007). In the present synthesis, the different morphologies of WO_3 hydrates were thus obtained in presence of these acids under hydrothermal reaction due to the different coordinating effects of the acids with tungsten species and their interaction with the selective crystal planes of the WO_3 hydrate nanoparticles controlling the growth of these planes in the preferential directions. Liu et al. (2008) also observed the change of the phase composition, crystal size, and microstructure of titania by hydrothermal synthesis using different carboxylic acids due to the coordinating effects of carboxylic acids with titanium ions and their adsorption on the surface of titania nanoparticles. However, the details of growth process of the different morphologies are not very clear at the present stage and need to be further studied.

The photocatalytic performance of the synthesized powders was investigated in photo-oxidation of water in PEC cells through fabrication of photoanodes. The film photoanode was fabricated by coating on FTO glass substrates. The XRD patterns of the WO_3 films cast onto the glass slides using the as-synthesized powders obtained from oxalic acid-assisted synthesis are shown in Fig. 4. The crystal structure as a function of annealing temperature was also investigated. The XRD patterns depict that the WO_3 film developed a monoclinic crystal phase annealing at 450 °C, as the majority of the peaks were well matched with the diffraction lines reported in JCPDS file (JCPDS 97-001-6080). Increasing peak height along with narrowing peak width was observed with increasing the annealing temperature from 450 to 600 °C, suggesting a higher degree of crystallinity in the film, and the crystal growth with the temperature. The crystallite size for WO_3 obtained from oxalic acid-assisted synthesis estimated from the Scherrer's equation using the (002) peak was found to be 43 nm when annealed at 450 °C, 46 nm at 500 °C, 48 nm at 550 °C, and 50 nm at 600 °C. Therefore, the crystallite size increased as the annealing temperature increased. However, this change is very small. There was no readily noticeable change in crystal structure of the WO_3 films detected with annealing temperatures. The influence of the annealing temperature on the photoelectrocatalytic activity was demonstrated using the WO_3 films annealed at different temperatures.

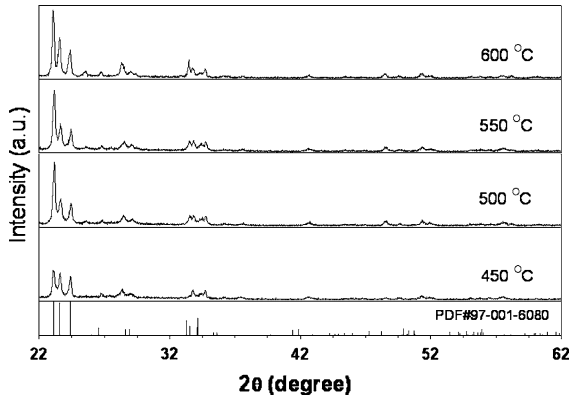

Fig. 4 XRD patterns of the WO_3 films after annealing at different temperatures. The films were coated on glass substrates using as-synthesized WO_3 hydrates prepared in the presence of oxalic acid

The XRD patterns of the WO_3 films derived from WO_3 hydrates obtained from the citric, oxalic, and tartaric acid-assisted synthesis routes and annealed at 500 °C in static air are displayed in Fig. 5. All the films exhibited similar diffraction patterns which were identified essentially with the crystalline monoclinic phase of WO_3 (JCPDS 97-001-6080). The crystallite sizes calculated from the Scherrer's equation using the (002) peak were 51, 46, and 43 nm for the WO_3 films obtained in presence of citric, oxalic, and tartaric acid, respectively. The order of the crystallite size offered an idea about the particle sizes assembled in the film on the FTO glass.

The slurry prepared for film fabrication was studied by thermal analysis. The TG analysis for the slurry

(S2b) clearly showed ~8% weight loss of up to 225 °C corresponding to the vaporization of absorbed water and a rapid weight loss of ~55% between 225 and 500 °C, attributed to the decomposition/oxidation of the organic faction in the slurry used as binder/dispersant. Beyond 500 °C the TGA curve showed no further weight loss. Emergence of two exothermic peaks in DTA curve also indicated the decomposition/oxidation of the organic portion in the slurry. The endothermic peak in the DTA curve below 225 °C corresponded to the dehydration process. Therefore, the organic mass was removed from the WO_3 films after annealing at 500 °C for 1 h.

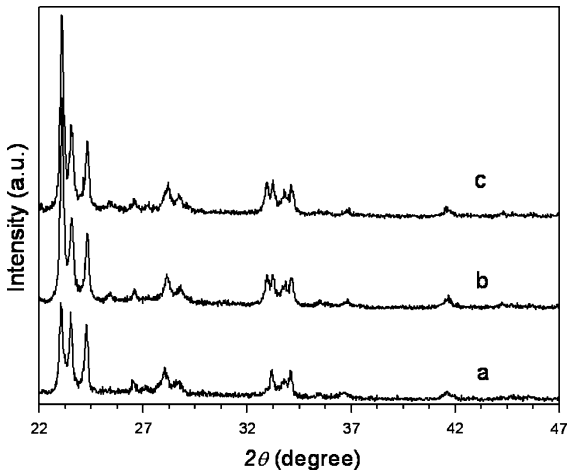

Fig. 5 XRD patterns of the WO_3 films prepared in the presence of *a* citric, *b* oxalic, and *c* tartaric acid and annealed at 500 °C for 1 h

The solid-state UV–visible spectral data recorded in the absorbance mode for the annealed WO_3 films obtained from oxalic acid-assisted synthesis and coated on glass substrates are shown in Fig. 6a. The optical properties of WO_3 in the visible region are dominated by the absorption threshold, which is defined by the band gap energy of the materials (Hjelm et al. 1996). The onset positions of light absorption for all films were found to be almost similar because of very small change in particle size of the materials with annealing temperature as was observed by XRD study of annealed films. However, this small change of the crystallite size was reflected on the UV–visible spectral data in the region of 300–425 nm wavelength with a red shift of absorption wavelength. The solid-state UV–visible spectral data for the WO_3 films obtained from oxalic, citric, and tartaric acid-controlled approaches and annealed at 500 °C for 1 h are presented in Fig. 6b. The absorption edges of all films annealed at 500 °C were very close in the range of 450–460 nm indicating the band gap energy value of 2.67–2.75 eV, which is in a good agreement with that reported for WO_3 (Hong et al. 2009). Therefore, that the different structure-directing agents did not affect the band gap energy of WO_3 systems notably was observed form UV–visible absorption spectra in this study.

The SEM micrographs (Fig. 7) of three types of WO_3 films obtained from oxalic, citric, and tartaric acid-assisted synthesis and coated on FTO glass substrates followed by annealing at 500 °C for 1 h showed a distinguishable difference in the surface morphology. Overall, all the films consisted of finer

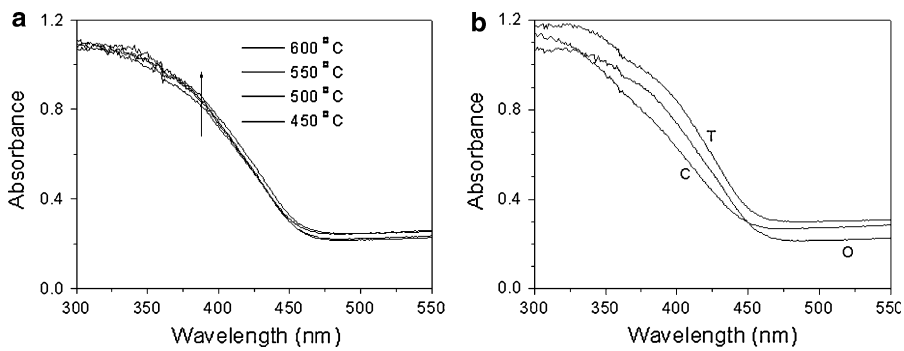

Fig. 6 UV–visible diffuse reflectance spectra of **a** the WO_3 films annealed at different temperatures after coating on FTO glass substrates using as-synthesized WO_3 hydrates prepared in the presence of oxalic acid and **b** the WO_3 films annealed at 500 °C after coating with as-synthesized WO_3 hydrates prepared in the presence of citric acid (*C*), oxalic acid (*O*), and tartaric acid (*T*)

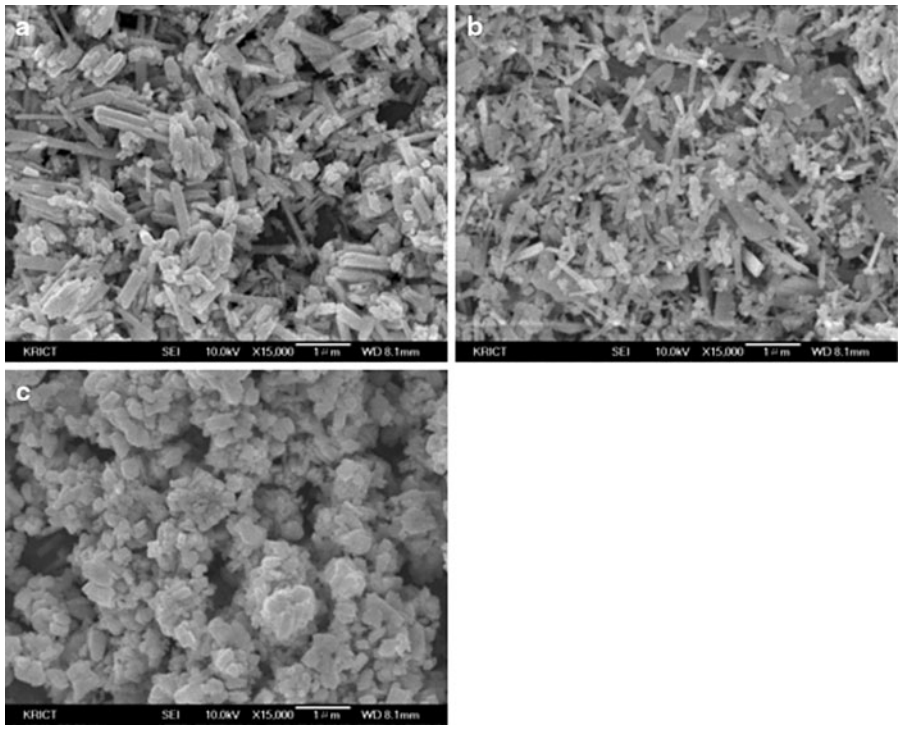

Fig. 7 SEM images of the WO_3 films annealed at different temperatures. The films were coated on FTO glass substrates using as-synthesized WO_3 hydrates prepared in the presence of **a** citric acid, **b** oxalic acid, and **c** tartaric acid

agglomerates/clusters irregularly distributed in size. The roughness with porous characteristics for all WO_3 films was observable. The film surface of WO_3 obtained from citric acid-assisted route comprised polydispersed sintered rod-like particles with varying size (Fig. 7a). The film surface of WO_3 obtained from oxalic acid-assisted route was also viewed constituting polydispersed nanorods, nanoparticles, and sintered particles (Fig. 7b). The film surface of WO_3 obtained from tartaric acid-assisted route exhibited clustered particles with a roughness (Fig. 7c). The microstructures of these film surfaces could be readily differentiated from SEM micrographs.

The as-synthesized WO_3 hydrate nanocrystals were implemented for the fabrication of photoanodes in PEC cells for photocatalytic water oxidation. Linear sweep voltammetry of all WO_3 films derived from WO_3 hydrate nanocrystals was performed for photooxidation of water under the illumination of AM 1.5G simulated solar light at 100 $mWcm^{-2}$ (1 sun) in 0.5 M H_2SO_4 (pH $\sim$0.3) solution. Figure 8 shows anodic current–voltage plots of the WO_3 films for the photooxidation of water in dark and in simulated sunlight at a scan rate of 50 mVs^{-1}; the WO_3 films were coated using the WO_3 hydrate synthesized in presence of oxalic acid and annealed at 450, 500, 550, and 600 °C for 1 h in air. In the dark, the anodic current for all the films annealed at different temperatures was hardly observed in the range of applied potential of 0.3–1.8 V from dark scan linear sweep voltammagrams (Fig. 8). Under illumination with solar light with intensity of 100 $mWcm^{-2}$ (1 sun), the anodic current was generated due to water oxidation. The onset of photocurrent began at around 0.4 V with respect to Ag/AgCl reference electrode. The photocurrent for all electrodes increased with increasing the positive potential due to the rapid separation of photogenerated electron–hole pairs under higher external bias potential. The WO_3 films obtained from oxalic acid-assisted synthesis exhibited a bell-shaped dependence of the photocurrent on the annealing temperatures, i.e., with increasing the annealing temperatures the photocurrent increased and reached maxima and then decreased. The oxalic acid-assisted synthesized films annealed at 450, 500, 550, and 600 °C showed the photocurrent and reached the value of 0.2, 0.77, 0.54, and 0.5 $mAcm^{-2}$,

respectively, with an external bias of 1.8 V versus Ag/AgCl electrode as observed in the chopped voltammagrams in Fig. 8. This behavior could be explained by considering volume recombination of electrons and holes (Hong et al. 2009). In the PEC system, the photogenerated electrons at photoanode upon illumination transport to conducting FTO glass substrate and the holes participate in water oxidation. The external potential leads to electron migration to the cathode which is the platinum counter electrode where hydrogen generation takes place. For the better PEC performance the film photoanode materials should possess high degree of crystalline nature, small amount of grain boundaries, and smaller crystal size to avoid/minimize the electro-hole recombination. Annealing process of the film photoanode assists in improving the degree of crystalline character and lowering the grain boundaries which are favorable for high photocurrent. The annealing process also enlarges the crystal size which causes lowering of the photocurrent by the electro-hole recombination. Therefore, there exists the optimum crystal size which is achieved by annealing at a suitable temperature for photoelectrochemical oxidation of water in PEC system. The highest photocurrent of 0.77 $mAcm^{-2}$ obtained in the present study is comparable to other reported values measured using 100 $mWcm^{-2}$ (AM 1.5G) simulated solar light (Hong et al. 2009; Jiao et al. 2011). Figure 9 shows anodic current–voltage plots of all the WO_3 films for the photooxidation of water in dark and in simulated sunlight at a scan rate of 50 mVs^{-1}. The WO_3 films were prepared using the WO_3 hydrates synthesized in presence of citric, oxalic and tartaric acid and annealed at 500 °C for 1 h in air. The photocurrents of the films with citric and tartaric acid assisting agents were 0.65 and 0.61 $mAcm^{-2}$ at 1.8 V versus Ag/AgCl, respectively. A higher photocurrent of WO_3 photoanode obtained by oxalic acid-mediated synthesis approach could be attributed to one-dimensional nanostructure with regular particle width and length. Figure 10

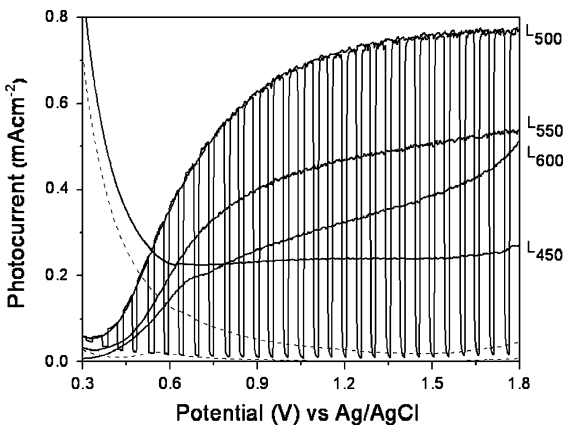

Fig. 8 Photocurrent–potential curve for the WO_3 films, prepared from oxalic acid-mediated products and annealed at different temperatures illuminated with AM 1.5 solar light (100 $mWcm^{-2}$) in 0.5 M H_2SO_4 (pH ~0.3) solution. *Uninterrupted lines* indicate photocurrents and *broken lines* indicate dark current. *L* stands for photocurrent

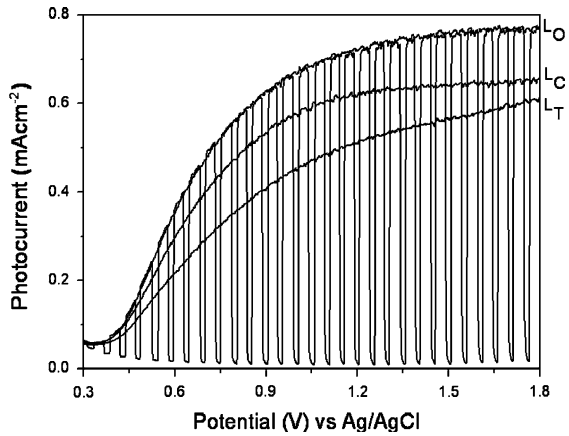

Fig. 9 Photocurrent–potential curve for the WO_3 films, prepared from oxalic (*O*), citric (*C*), and tartaric acid (*T*) mediated products illuminated with AM 1.5 solar light (100 $mWcm^{-2}$) in 0.5 M H_2SO_4 (pH ~0.3) solution. *L* stands for photocurrent

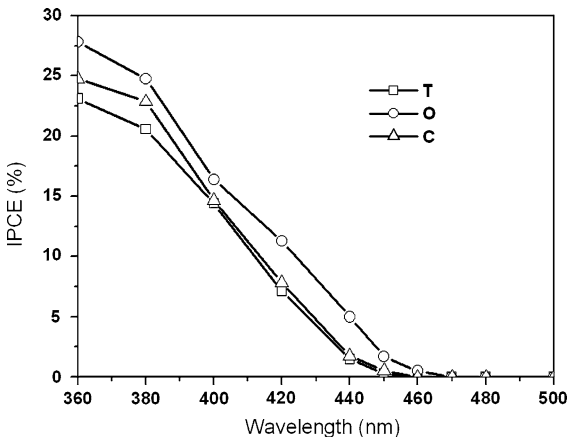

Fig. 10 IPCE plots for the WO_3 films, prepared from oxalic (*O*), citric (*C*), and tartaric acid (*T*) in 0.5 M H_2SO_4 (pH ~0.3) solution with a bias of 1.2 V versus Ag/AgCl

depicts IPCE of the WO_3 photoanodes at 1.2 V (vs. Ag/AgCl) at pH $\sim$0.3. The IPCE (%) was obtained from the equation, IPCE (%) $= (1{,}240I/\lambda)P \times 100$, where I represents photocurrent ($mAcm^{-2}$), P and λ correspond to light intensity ($mWcm^{-2}$), and wavelength (nm) of incident monochromatic light, respectively. The photocurrent results were found to be consistent with IPCE results. The onset of IPCE was observed at 460–470 nm. The light with wavelength longer than 480 nm cannot be absorbed due to intrinsic band gap energy of WO_3 (Hong et al. 2009).

Conclusions

In summary, we have developed an easy, economical, and environment friendly method for the production of rod- and plate-like morphologies of WO_3 nanocrytals. Different organic acids such as oxalic, citric, and tartaric acid have been used as structure-directing agents. Detailed characterization shows the as-synthesized products are WO_3 hydrate with orthorhombic crystal structure which transform to the hexagonal WO_3 through dehydration upon heating at 350 °C for 5 h. The orthorhombic crystal phase, obtained by post annealing, retains its phase stability at room temperature. SEM and TEM study show that the oxalic acid-mediated synthesis produces predominantly rod-like morphology of the WO_3 hydrates with high-aspect ratio, the citric acid-assisted synthesis results in nanosized rod-shaped particles with some nanosheet patterns and the tartaric acid-controlled synthesis produces nanoplate morphology with wide and flat surface. The photocurrent measurements exhibit obvious photocatalytic activity with a photocurrent of about 0.77, 0.61, and 0.65 $mAcm^{-2}$ for the WO_3 film derived with the oxalic acid, the tartaric- and citric acid-assisting agents, respectively, at 1.8 V versus Ag/AgCl electrode in the presence of illumination of AM 1.5G simulated solar light (100 $mWcm^{-2}$). The photocurrent results were found to be consistent with IPCE results. The onset of IPCE was observed at 460–470 nm. The PEC performance of WO_3 photoanodes depends on microstructural properties and morphologies of the films.

Acknowledgments This research (paper) has been done for the Hydrogen Energy R&D Center that is one of the twenty-first century Frontier R&D Programs funded by the Ministry of Science and Technology, Republic of Korea.

References

Amano F, Lib D, Ohtani B (2010) Fabrication and photoelectrochemical property of tungsten(VI) oxide films with a flake-wall structure. Chem Commun 46:2769–2771

Bamwenda G, Arakawa H (2001) The visible light induced photocatalytic activity of tungsten trioxide powders. App Catal A Gen 210:181–191

Boukriba M, Sediri F, Gharbi N (2010) Hydrothermal synthesis of $WO_3.1/3H_2O$ nanorods and study of their electrical properties. Polyhedron 29:2070–2074

Butler MA (1977) Photoelectrolysis and physical properties of the semiconducting electrode WO_3. J Appl Phys 48: 1914–1920

Gu Z, Ma Y, Yang W, Zhang G, Yao J (2005) Self-assembly of highly oriented one-dimensional h-WO_3 nanostructures. Chem Commun 3597–3599

Hjelm A, Granqvist CG, Wills JM (1996) Electronic structure and optical properties of WO_3, $LiWO_3$, $NaWO_3$, and HWO_3 Phys. Rev B 54:2436–2445

Hodes G, Cahen D, Manassen J (1976) Tungsten trioxide as a photoanode for photoelectrochemical cell (PEC). Nature 260:312–313

Hong SJ, Jun H, Borse PH, Lee JS (2009) Size effects of WO_3 nanocrystals for photooxidation of water in particulate suspension and photoelectrochemical film systems. Int J Hydrogen Energy 34:3234–3242

Jiao Z, Wang J, Ke L, Sun XW, Demir HV (2011) Morphology-tailored synthesis of tungsten trioxide (hydrate) thin films and their photocatalytic properties. ACS Appl Mater Interfaces 3:23–229

Kominami H, Yabutani K, Yamamoto T, Kera Y, Ohtani B (2001) Synthesis of highly active tungsten(VI) oxide photocatalysts for oxygen evolution by hydrothermal treatment of aqueous tungstic acid solutions. J Mater Chem 11:3222–32227

Lassner E, Schubert WD (1999) Tungsten: properties, chemistry, technology of the element, alloys, and chemical compounds. Springer, Berlin

Lee K, Seo WS, Park JT (2003) Synthesis and optical properties of colloidal tungsten oxide nanorods. J Am Chem Soc 125:3408–3409

Lee SH, Deshpande R, Parilla PA, Jones KM, To B, Mahan AH, Dillon AC (2006) Crystalline WO_3 nanoparticles for highly improved electrochromic applications. Adv Mater 18: 763–766

Li XL, Liu JF, Li YD (2003) Large-scale synthesis of tungsten oxide nanowires with high aspect ratio. Inorg Chem 42:921–924

Li XL, Lou TJ, Sun XM, Li YD (2004) Highly sensitive WO_3 hollow-sphere gas sensors. Inorg Chem 43:5442–5449

Lin HM, Hsu CM, Yang HY, Lee PY, Yang CC (1994) Nanocrystalline WO_3-based H_2S sensors. Sens Actuators B 22: 63–68

Liu Y, Liu CY, Zhang ZY (2008) Effects of carboxylic acids on the microstructure and performance of titania nanocrystals. Chem Eng J 138:596–601

Llopis E, Ramirez JA, Cervilla A (1986) Tungsten (VI)-gluconic acid complexes: polarimetric and ^{13}C-n.m.r. studies in an excess of tungsten (VI). Transition Met Chem 11:489–494

Michailovski A, Krumeich F, Patzke GR (2004) Hierarchical growth of mixed ammonium molybdenum/tungsten bronze nanorods. Chem Mater 16:1433–1440

Rajagopal S, Nataraj D, Mangalaraj D, Djaoued Y, Robichaud J, Khyzhun OY (2009) Controlled growth of WO_3 nanostructures with three different morphologies and their structural, optical, and photodecomposition studies. Nanoscale Res Lett 4:1335–1342

Santato C, Ulmann M, Augustynski J (2001) Photoelectrochemical properties of nanostructured tungsten trioxide films. J Phys Chem B 105:936–940

Su J, Feng X, Sloppy JD, Guo L, Grimes CA (2011) Vertically aligned WO_3 nanowire arrays grown directly on transparent conducting oxide coated glass: synthesis and photoelectrochemical properties. Nano Lett 11:203–208

Takeda Y, Kato N, Fukano T, Takeichi A, Motohiro T, Kawai S (2004) WO_3/metal thin-film bilayered structures as optical recording materials. J Appl Phys 96:2417–2422

Wang H, Lindgren T, He J, Hagfeldt A, Lindquist SE (2000) Photoelectrochemistry of nanostructured WO_3 thin film electrodes for water oxidation: mechanism of electron transport. J Phys Chem B 104:5686–5696

Xiong YJ, Xia YN (2007) Shape-controlled synthesis of metal nanostructures: the case of palladium. Adv Mater 19: 3385–3391

Zhao ZG, Miyauchi M (2008) Nanoporous-walled tungsten oxide nanotube as highly active visible-light-driven photocatalysts. Angew Chem Int Ed 47:7051–7055

Zhao ZG, Liu ZF, Miyauchi M (2010) Nature-inspired construction, characterization, and photocatalytic properties of single-crystalline tungsten oxide octahedral. Chem Commun 46:3321–3323

Zheng H, Tachibana Y, Kalantar-zadeh K (2010) Dye-sensitized solar cells based on WO_3. Langmuir 26:19148–19152

Zheng H, Ou JZ, Strano MS, Kaner RB, Mitchell A, Kalantar-zadeh K (2011) Nanostructured tungsten oxide—properties, synthesis, and applications. Adv Funct Mater 21: 2175–2196

Zhou L, Zou J, Yu M, Lu P, Wei J, Qian Y, Wang Y, Yu C (2008a) Green synthesis of hexagonal-shaped $WO_3 \cdot 0.33H_2O$ nanodiscs composed of nanosheets. Cryst Growth Des 8:3993–3998

Zhou L, Wang W, Xu H (2008b) Controllable synthesis of three-dimensional well-defined $BiVO_4$ mesocrystals via a facile additive-free aqueous strategy. Cryst Growth Des 8: 728–733

Zhu J, Wang S, Xie S, Li H (2011) Hexagonal single crystal growth of WO_3 nanorods along a [110] axis with enhanced adsorption capacity. Chem Commun 47:4403–4405